AIP Journal of Applied Physics

A study on Si/Al2O3 paramagnetic point defects

S. Kühnhold-Pospischil, P. Saint-Cast, M. Hofmann, S. Weber, P. Jakes, R.-A. Eichel, and J. Granwehr

Citation: Journal of Applied Physics **120**, 195304 (2016); doi: 10.1063/1.4967919
View online: http://dx.doi.org/10.1063/1.4967919
View Table of Contents: http://scitation.aip.org/content/aip/journal/jap/120/19?ver=pdfcov
Published by the AIP Publishing

A study on Si/Al_2O_3 paramagnetic point defects

S. Kühnhold-Pospischil,[1,2,3] P. Saint-Cast,[1] M. Hofmann,[1] S. Weber,[2] P. Jakes,[4] R.-A. Eichel,[4,5] and J. Granwehr[4,6]
[1]*Fraunhofer Institute for Solar Energy Systems ISE, Heidenhofstr. 2, 79110 Freiburg, Germany*
[2]*Institut für Physikalische Chemie, Albert-Ludwigs-Universität Freiburg, Albertstr. 21, 79104 Freiburg, Germany*
[3]*Freiburg Materials Research Center FMF, Albert-Ludwigs-Universität Freiburg, Stefan-Meier-Str. 21, 79104 Freiburg, Germany*
[4]*Forschungszentrum Jülich, Institute of Energy and Climate Research, IEK-9, 52425 Jülich, Germany*
[5]*RWTH Aachen University, Institut für Physikalische Chemie, 52074 Aachen, Germany*
[6]*RWTH Aachen University, Institut für Technische und Makromolekulare Chemie, 52074 Aachen, Germany*

(Received 15 September 2016; accepted 3 November 2016; published online 18 November 2016)

In this contribution, negative charges and electronic traps related to the Si/Al_2O_3 interface were measured and related to paramagnetic point defects and molecular vibrations. To this end, contactless capacitance voltage measurements, X-band electron paramagnetic resonance (EPR), and infrared spectroscopy were carried out, and their results were compared. A change in the negative charge density and electron trap density at the Si/Al_2O_3 interface was achieved by adding a thermally grown SiO_2 layer with varying thicknesses and conducting an additional temperature treatment. Using EPR, five paramagnetic moments were detected in $Si/(SiO_2)/Al_2O_3$ samples with g values of $g_1 = 2.0081 \pm 0.0002$, $g_2 = 2.0054 \pm 0.0002$, $g_3 = 2.0003 \pm 0.0002$, $g_4 = 2.0026 \pm 0.0002$, and $g_5 = 2.0029 \pm 0.0002$. Variation of the Al_2O_3 layer thickness shows that paramagnetic species associated with g_1, g_2, and g_3 are located at the Si/Al_2O_3 interface, and those with g_4 and g_5 are located within the bulk Al_2O_3. Furthermore, g_1, g_2, and g_3 were shown to originate from oxygen plasma exposure during Al_2O_3 deposition. Comparing the g values and their location within the Si/Al_2O_3 system, g_1 and g_3 can be attributed to P_{b0} centers, g_3 to Si dangling bonds (Si-dbs), and g_4 and g_5 to rotating methyl radicals. All paramagnetic moments observed in this contribution disappear after a 5-min temperature treatment at 450°C. The deposition of an additional thermal SiO_2 layer between the Si and the Al_2O_3 decreases the negative fixed charge density and defect density by about one order of magnitude. In this contribution, these changes can be correlated with a decrease in amplitude of the Si-db signal. P_{b0} and the methyl radical signals were less affected by this additional SiO_2 layer. Based on these observations, microscopic models for the negative fixed charge density (Q_{tot}) and the interface trap density (D_{it}) and the connection between these values are proposed. *Published by AIP Publishing.* [http://dx.doi.org/10.1063/1.4967919]

I. INTRODUCTION

Plasma-enhanced atomic layer deposited (PE-ALD) Al_2O_3 on crystalline silicon (*c*-Si) can deliver outstanding surface passivation qualities.[1,2] For the last ten years, PE-ALD Al_2O_3 has been investigated in detail for application in highly efficient *p*- and *n*-type Si photovoltaic cell concepts, such as Passivated Emitter and Rear Cells (*PERC*),[3–5] Passivated Emitter with Rear Locally diffused (*PERL*) cells,[6] and as high-*k* materials for metal oxide semiconductor (MOS) structures.[7] To date, Al_2O_3 is frequently used in the photovoltaics industry for surface passivation.[1]

Al_2O_3 passivates the Si surface by one of the two mechanisms: one is based on the saturation of traps at the Si/Al_2O_3 interface, which is called *chemical passivation*, and the other is based on the band bending induced by negative fixed charges at the Si/Al_2O_3 interface, which is called *field effect passivation*.[8,9] To activate the passivation of PE-ALD Al_2O_3 layers, an adequate temperature treatment is required. After deposition, the interface trap density is around $D_{it} \approx 10^{13}\,eV^{-1}cm^{-2}$. During the annealing process, D_{it} decreases to values of approximately $10^{11}\,eV^{-1}cm^{-2}$. This decrease is most likely caused by the formation of a thin SiO_x layer at the Si/Al_2O_3 interface combined with the saturation of interfacial traps by hydrogen. It was shown by Fourier-transform infrared spectroscopic (FTIR) measurements that both oxygen and hydrogen diffuse towards the interface during annealing.[10] The negative fixed charge density at the interface Q_{tot} is already quite high ($Q_{tot} \approx 10^{12}\,cm^{-2}$) after deposition and increases only slightly to a value of about $Q_{tot} \approx 5 \times 10^{12}\,cm^{-2}$ during annealing.[1]

The microscopic nature behind D_{it} and Q_{tot} is still a matter of discussion.[1] The D_{it} resembles quantum states energetically located within the band gap. These quantum states may arise from material impurities, point defects, or both. In addition, Q_{tot} might be related to specific point defects at the Si/Al_2O_3 interface. Promising candidates are dangling bonds, aluminum vacancies, or oxygen interstitials, which may act as deep acceptor traps for electrons.[1,11,12] Indeed, a correlation between a slightly enriched oxygen interstitial concentration and Q_{tot} at the Si/Al_2O_3 interface has been reported.[13] Moreover, an enhanced concentration of tetrahedral AlO_4 sites compared to octahedral AlO_6 sites was reported for Si/Al_2O_3 interfaces, which might also correlate with the appearance of negative fixed charges.[9,14–16]

TABLE I. Compilation of paramagnetic defects in Si/Al_2O_3 measured with cw-X Band EPR (in Dingemans and Kessels and in Baldovino *et al.*; the EDMR method was used).[1,27]

Dangling bond	g value	Field to sample orientation	Al_2O_3 thickness (nm)	Measurement temp. (K)	Ref.
P_{b0}	$g_1 = 2.0087$, $g_2 = g_3 = 2.0036$	$B\|\|[011]$		4	1
P_{b0}	$g_1 = 2.0059$	$B\|\|[100]$	15	RT	25
P_{b0}	$g_1 = 2.0024$, $g_2 = g_3 = 2.0074$	$B\|\|[100]$, $B\|\|[111]$, $B\|\|[110]$	11	RT	27
P_{b0}	$g_1 = g_2 = g_3 = 2.0062$, $g_1 = 0$, $g_2 = 2.0017$, $g_3 = 2.0077$, $g_1 = 2.0041$, $g_2 = g_3 = 2.0087$	$B\|\|[001]$, $B\|\|[111]$, $B\|\|[110]$	4	4 and 20	26
P_{b1}	$g_1 = 2.0037$	$B\|\|[100]$	15	RT	25
P_{b1}	Identical for all field orientations $g_1 = 2.0034$, $g_2 = 2.0051$, $g_3 = 2.0062$	$B\|\|[001]$, $B\|\|[111]$, $B\|\|[110]$	4	4 and 20	26
Si-db	$g = 2.0056$	$B\|\|[100]$, $B\|\|[111]$	15	RT	25
Si-db	$g = 2.0055$	$B\|\|[011]$		4	1
Si-db	$g = 2.0056 - 2.0059$	$B\|\|[001]$, $B\|\|[111]$, $B\|\|[110]$	4	4 and 20	26
E'-like	$g = 1.999$	$B\|\|[011]$		4	1

Interestingly, Q_{tot} is lower with the addition of a thermally grown interfacial SiO_2 layer, as was published by Dingemans *et al.* and Mack *et al.*[17,18] To explain this, Mack *et al.* suggested an electron transfer mechanism from Si via interface defects, leading to Q_{tot}. Thus, at least a part of D_{it} might deliver defects for electron transport.[19] Thus, D_{it} and Q_{tot} might be correlated.[19]

If electron transport causes Q_{tot}, one might expect Q_{tot} to be paramagnetic. However, no correlation between paramagnetic moments in Si/Al_2O_3 and the Q_{tot} concentration has been detected so far.[1] The existence of a negative correlation energy, often just called *negative U*, is a possible explanation for this observation.[20,21] Here, the occupation of two electrons in a single defect site is energetically preferable. In this case, no paramagnetic moments exist. Such negative *U centers* are well known for SiO_2 gate oxides and SiN_x and SiC films on Si.[22–24] Moreover, such double chargeable sites were suggested for oxygen interstitials in Si/Al_2O_3.[11] An experimental proof is still missing.

Most likely, at least some of the D_{it} at the Si/Al_2O_3 interface correspond to paramagnetic defects.[1] Thus, to study the microscopic nature behind D_{it} and its possible relation to Q_{tot}, electron paramagnetic resonance (EPR) measurements are of great interest for Si/Al_2O_3 structures. Several reports on EPR studies of PE-ALD Al_2O_3 on *c*-Si have been published, in which the existence of P_{b0}, Si-db, and E'-like defects known from Si/SiO_2 interfaces was proposed.[1,25–28] P_{b0} indicates an anisotropic defect attributed to the Si/SiO_2 interface where a Si atom is back bonded to three Si atoms, and an oxygen atom is missing, leading to the paramagnetic moment originating from the unpaired electron. P_{b0} defects were produced by the exposure of Si/SiO_2 samples with high energetic photons.[29] P_{b0} defects usually appear on the (100) wafer oriented crystal surfaces. E'-like defects are isotropic defects that are attributed to the SiO_2 bulk layer itself. Here, a Si atom is back bonded to three oxygen atoms, and again, one oxygen atom is missing. Furthermore, another isotropic defect, Si-db, has often been reported for Si/Al_2O_3 systems and is suggested to be located on the Si wafer surface.[1] Si-db can be correlated with amorphous Si.[30] Thus, this defect can be assigned to mechanical surface damages.[30] A summary of the g values associated with the dangling bonds discussed so far and some experimental details are given in Table I. After a temperature treatment, all paramagnetic moments listed in Table I disappear. This can be explained by the saturation of P_{b0} and Si-db by hydrogen.

As discussed above, the microscopic nature of D_{it} and Q_{tot} at the Si/Al_2O_3 interface is still unknown. It is possible that D_{it} and Q_{tot} are connected to each other. To obtain a deeper understanding of D_{it}, Q_{tot}, and the possible connection between these values, the concentrations of D_{it} and Q_{tot} between Si and Al_2O_3 were varied, and these samples were analyzed using contactless capacitance voltage measurements, EPR, and IR spectroscopies. The variations in D_{it} and Q_{tot} were achieved using an additional interfacial SiO_2 layer between Si and Al_2O_3 and by a temperature treatment. Moreover, to study the locations of paramagnetic moments within the $Si/(SiO_2)/Al_2O_3$ system, EPR studies were carried out on Si/Al_2O_3 samples with varying Al_2O_3 layer thicknesses. In addition, the impacts of oxygen plasma exposure on the Al_2O_3 EPR spectra were investigated. Based on these studies, a microscopic model for D_{it}, Q_{tot}, and the connection between these values in Si/Al_2O_3 is postulated.

II. EXPERIMENTAL AND SIMULATION

The experimental design is shown in Figure 1. After wet chemical cleaning, the thermal-oxide and PE-ALD depositions were carried out. For thermal-oxide growth, a tube furnace *E 2000 XL* from *Centrotherm Photovoltaics* was used. The PE-ALD deposition was carried out using the commercial ALD tool *OPAL* from *Oxford Instruments*. Here, the Al_2O_3 is deposited on both sides of the Si wafer by alternating trimethyl aluminium (TMAl) flux and oxygen plasma. The substrate temperature was 180 °C, the oxygen plasma step duration was set to 2.5 s, and the oxygen plasma power was 140 W. As the Si substrate material, 4 in., 100 Ω cm *p*-type monocrystalline wafers with shiny etched surfaces and (100) oriented Si crystal were used. The wafers were fabricated by applying the float zone method.

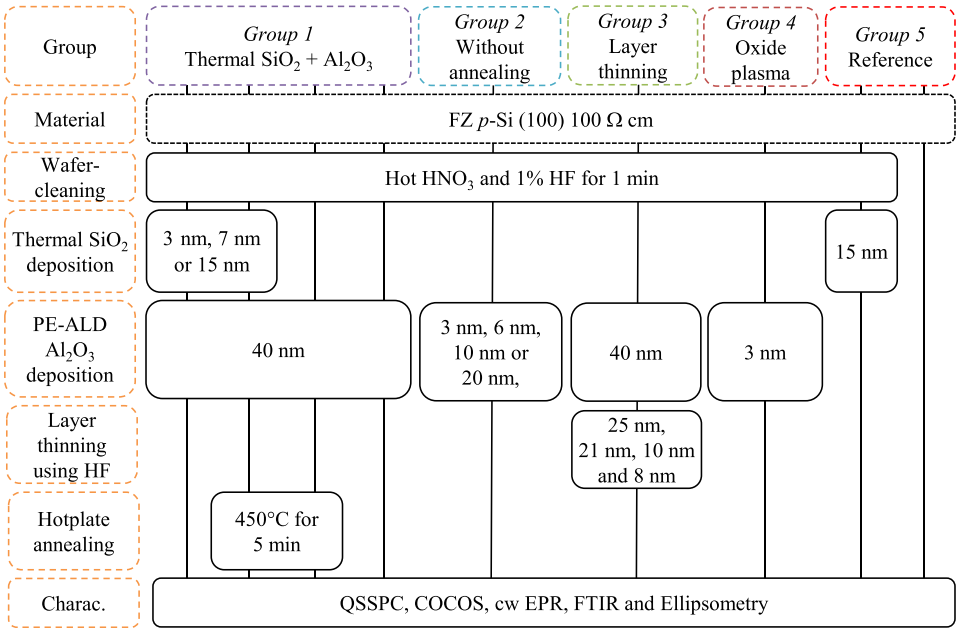

FIG. 1. Experimental flow.

For *Group 1* (see Figure 1), a thermal oxide layer with a thickness of 15 nm was first deposited onto the Si wafer. For some of the wafers, the original layer thickness was reduced to 3 nm and 7 nm using diluted hydrofluoric acid (HF). The three layer thicknesses (3 nm, 7 nm, and 15 nm) were then capped by an Al_2O_3 layer with a thickness of 40 nm. All wafers with layer thickness variations were manually split using a diamond cutter. One half of the wafers was annealed for 5 min at 450 °C using a hotplate in ambient air, and the other half was investigated without subsequent annealing.

Using different deposition times, five Al_2O_3 layer thicknesses, namely, 3 nm, 6 nm, 10 nm, 20 nm, and 40 nm, were deposited and studied in *Group 2*.

In *Group 3*, first, a 40 nm Al_2O_3 layer was deposited onto the Si wafer. Using HF, the original layer thickness was reduced to 8 nm, 10 nm, 21 nm, and 25 nm.

In *Group 4*, a 3 nm Al_2O_3 layer was exposed to an oxygen plasma treatment using the same plasma process parameters (temperature 180 °C, duration 2.5 s, and microwave power 140 W) as if a 40 nm Al_2O_3 layer would be deposited on the Si wafer without using TMAl between the oxygen plasma deposition steps.

In *Group 5*, two Si wafers were studied: one was coated with a single 15 nm SiO_2 layer, and the second did not have any layer.

All groups were characterized using the characterization methods listed below.

The layer thicknesses and refractive indices were determined by spectral ellipsometry using a *Spectral Ellipsometer* from *A. J. Woollam Co. Inc.* (*M-2000F*).[31–33] The measured data were analyzed using the *Cauchy Model*.[34] The thickness uncertainties are mainly given by the layer inhomogeneities, which are around 4%.[35] The refractive index at 600 nm is around $n = 1.4$ for the thermal SiO_2 and around $n = 1.6$ for the PE-ALD Al_2O_3 layers used in this contribution.

A contactless capacitance voltage measurement method called Corona Oxide Characterization of Semiconductors (COCOS) from *Semilab* (*PV2000*) was used to determine D_{it} and Q_{tot}.[36] Each data point represents two measurements. The maximum error for the COCOS measurements was deduced by Schuldis *et al.*, resulting in an error of 25% for D_{it} at mid-gap and around 10% for Q_{tot}.[37,38]

Quasi Steady State Photo-Conductance (QSSPC) measurements were applied to extract the effective carrier lifetimes using a *Sinton lifetime tester* (*WCT 120*).[39] Each data point consists of two measurements. The error was 11%, which was deduced by Blum *et al.*[40]

For X-Band EPR measurements, an EMX spectrometer from *Bruker Biospin* was used. Magnetic-field strengths around $B_0 \approx 350$ mT and microwave frequencies around 9.8 GHz (X-band) were applied using a *Super High Q* resonator (*ER4122SHQ*) from *Bruker Biospin*. The baseline was corrected for all spectra by subtracting a second-order polynomial.

The *Q-value* of the resonator can be understood as the fraction of stored energy over dissipated energy within the resonator, which is directly related to the sensitivity of detection. In the experiments discussed here, the Q value was in the range of 2600 to 2800 at a microwave power of around 19.97 mW. An empty cavity has a Q-value of around 7000. The losses in Q upon insertion of the Si-based samples can be rationalized by the Si's absorption of microwaves in the resonator. Thus, Q depends on the amount of samples loaded into the resonator. Attempts were made to keep the Q value constant for all measurements, but the error in the Q value detection is around 30%. Thus, a maximum error in amplitude of 30% is assumed.

To minimize the loss in Q, a high-ohmic Si material was used (100 Ωcm). Nevertheless, microwave absorption cannot fully be avoided at room temperature. Thus, the samples absorb microwaves, leading to the evolution of heat, which results in a shift in frequency during the measurements.

To compare the signal amplitudes and g values among the samples, all spectra were normalized using the sample weights, which were typically in the range of 1.18 g to 1.19 g per sample (one sample comprises around 12 Si stripes with

widths of ∼2.3 mm, lengths of ∼2 cm, and their respective thin layer system).

For magnetic-field calibration, a Li:LiF standard was used, which reveals an error as small as $\Delta g \approx 1 \times 10^{-7}$.[41] Nevertheless, the uncertainty in the detection of a g-value is dominated by the uncertainties in the magnetic-field detection (by a Hall probe) and the microwave frequency detection. Calculating the standard deviation over six measurements delivers a maximum error in g of approximately $\Delta g = 2 \times 10^{-4}$. This error was applied to all g values estimated in this contribution. For the EPR measurements, all samples were cut into adequately sized stripes, as previously discussed, and placed into quartz EPR tubes. During the measurements, the magnetic field was oriented parallel to the [010] crystal orientation of the wafer. To simulate EPR spectra, the software *Matlab* using the toolbox *EasySpin* was applied.[42]

In addition, FTIR modes of molecular vibrations were extracted by Fourier transform infrared spectroscopy (FTIR) using an *IFS* 113 V from *Bruker*. Due to an internal wavenumber calibration, a maximum error of three wavenumbers is assumed. The software called *Fityk 0.9.8* was used to fit all FTIR peaks with Gaussian shapes.[43]

III. RESULTS

Values for D_{it}, Q_{tot}, and the effective carrier lifetime (τ_{eff}) obtained from the *Group 1* samples using the COCOS and QSSPC characterization methods before and after annealing are shown in Figure 2. D_{it} decreases with increasing SiO_2 layer thickness for both the unannealed and annealed samples. Furthermore, improvements in τ_{eff} after hotplate annealing

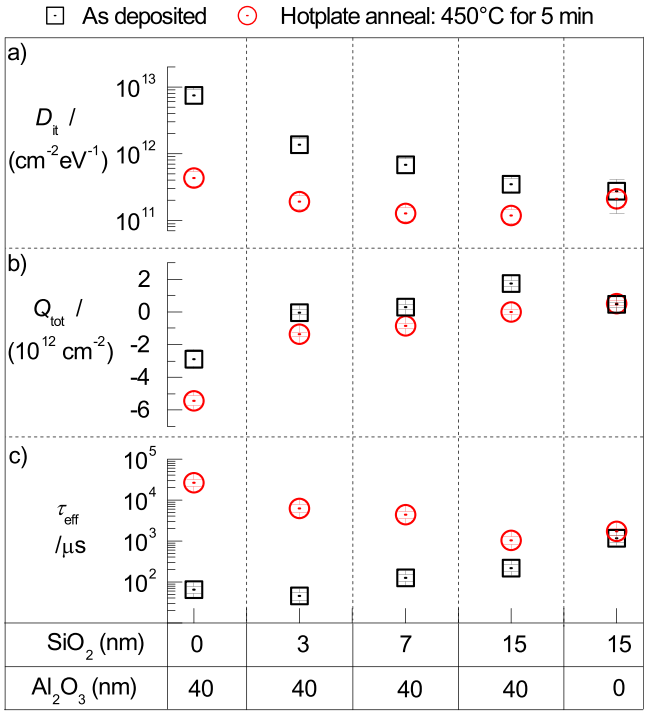

FIG. 2. D_{it} (a), Q_{tot} (b), and τ_{eff} (c) of $Si/SiO_2/Al_2O_3$ stacks with and without annealing are presented as functions of SiO_2 layer thickness (*Group 1*). For reference, a single 15 nm SiO_2 layer (right) is shown (*Group 5*).

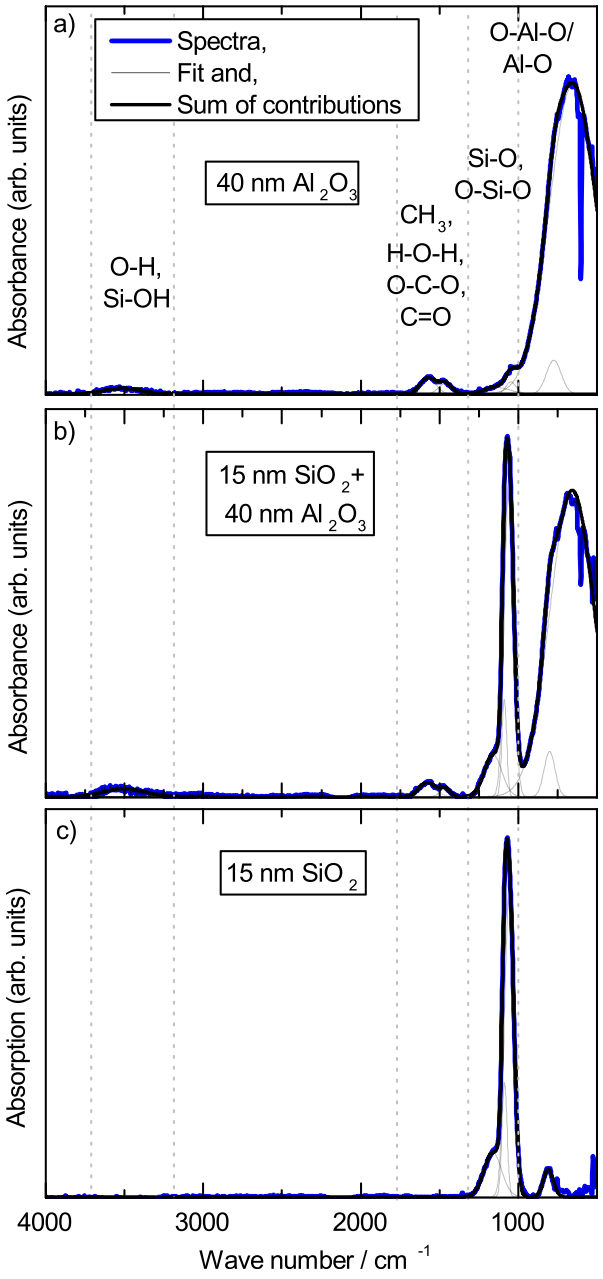

FIG. 3. FTIR spectra of (a) a single Al_2O_3 layer with a 40 nm layer thickness on Si after annealing (*Group 1*) (b) Si stacked with 15 nm SiO_2 and 40 nm Al_2O_3 after annealing (*Group 1*), and (c) a single SiO_2 layer with a 15 nm layer thickness on Si (*Group 5*).

become smaller with increasing SiO_2 layer thickness. Moreover, for both the SiO_2 layer without any Al_2O_3 layer and the Al_2O_3 layer without any SiO_2 reveal relatively high D_{it} concentration after annealing. The absolute values of Q_{tot} and D_{it} decrease with increasing SiO_2 layer thickness, and Q_{tot} becomes positive for SiO_2 without any Al_2O_3 after annealing. Similar data have already been published by Dingemans and Kessels and Mack *et al.*[1,18] A high τ_{eff} correlates with low D_{it} and high Q_{tot} values. Thus, the effective carrier lifetime decreases with increasing SiO_2 layer thickness after annealing. After annealing, the longest effective lifetimes can be achieved for the single Al_2O_3 layer without any thermal SiO_2 interfacial layer.

TABLE II. Summary of wave numbers, their corresponding molecules and surroundings observed in $Si/(SiO_2)/Al_2O_3$ samples (after Kühnhold *et al.*).[16]

Wave number (cm^{-1})	Molecule	Vibrational mode	Surrounding	Reference
400 – 530	Al – O	Stretching	Octahedral matrix	45–49
600 – 900		Optical phonon	SiO_2	52
650 – 700	O – Al – O	Bending	Octahedral and tetrahedral matrix	45–50
750 – 850	Al – O	Stretching	Tetrahedral matrix	45–50
900 – 1200	Si – O, O – Si – O	Stretching	SiO/SiO_2	50 and 51
1900 – 1200	H – O – H, O – C – O, CH_3, $C=O$	Asym. vibrations		54–58
1100 – 1300		Optical phonon	SiO_2	52, 53
1300 – 1750	H – O – H	Bending	Tetrahedral and octahedral γ-Al ions	48
2330 – 2340	O – C – O	Stretching	Al_2O_3	47
2600 – 3800	O – H	Stretching	Al – OH	48
3000 – 3600	Si – OH	Stretching		50

FTIR spectra taken from a Si sample coated with a single Al_2O_3 layer with a thickness of 40 nm (*Group 1*), a sample with a SiO_2 layer and an Al_2O_3 layer with thicknesses of 15 nm and 40 nm, respectively (*Group 1*), and a sample with a single SiO_2 layer with a thickness of 15 nm (*Group 5*) are shown for example, in Figure 3. Spectra (a) and (b) were taken after annealing. However, identical results were obtained directly after deposition (not shown here). In Figures 3(a) and 3(b), the known peaks from Al_2O_3 were observed and summarized briefly (see also Table II).[16,44] The broad peak at a maximum wavenumber of around 670 cm^{-1} consists of O-Al-O bending modes (650 cm^{-1} – 700 cm^{-1}), Al-O stretching modes for Al-O in octahedral matrices (400 cm^{-1} –530 cm^{-1}), and Al-O stretching modes in tetrahedral and octahedral matrices (750 cm^{-1} – 850 cm^{-1}).[45–50] The peak around 900 cm^{-1} – 1300 cm^{-1} is assigned to Si-O and O-Si-O stretching modes and optical phonon modes.[50–53] At around 1300 cm^{-1} – 1750 cm^{-1}, the two peaks can be related to asymmetric vibration modes of H-O-H, O-C-O, and C = O.[54–58] The feature at 3000 cm^{-1} – 3800 cm^{-1} can be assigned to Si-OH and O-H stretching modes.[16,44] In Figure 3(b), the strong peak from the additional interfacial SiO_2 layer can be seen in the range of 900 cm^{-1} – 1300 cm^{-1}.[48,50] In Figure 3(c), an FTIR spectrum of a single thermally grown SiO_2 layer is shown; the feature around 600 cm^{-1} – 900 cm^{-1} can be assigned to optical phonon vibrations in SiO_2.[52,53]

EPR measurements were carried out to study the differences in the defect structures of the Si/Al_2O_3 samples with and without additional thermally grown SiO_2 layers (*Group 1*). EPR spectra obtained for a sample with 40 nm of Al_2O_3 without annealing and without an additional SiO_2 layer are shown in Figure 4(a) as examples (*Group 1*). The spectra can be simulated by summing up the signals from the paramagnetic moments already known from the PE-ALD Al_2O_3 samples, namely, P_{b0} (g_1 and g_3) and Si-db (g_2), an additional hyperfine coupling (g_4), and another broad peak (g_5), as indicated by the black line in Figure 4(a). The individual contributions of the simulation are indicated by thin black lines, and the hyperfine coupling is indicated by a dashed magenta line. All other spectra studied in this contribution (*Group 1* to *Group 4*) have been simulated analogously. After an annealing treatment of 450 °C for 5 min, all contributions disappear, as shown in Figure 4(b). Here, samples with 15 nm of SiO_2 and 40 nm of Al_2O_3 are compared after annealing (*Group 5*). The SiO_2 and annealed Al_2O_3 signals are identical and relatively small. In addition, also Si without any layer reveals an identical spectrum (not shown here). Thus, these signals can be understood as resonator background.

The simulations revealed identical g values for all groups without a temperature treatment. These g values are $g_1 = 2.0081 \pm 0.0002$, $g_2 = 2.0054 \pm 0.0002$, $g_3 = 2.0003 \pm 0.0002$, $g_4 = 2.0026 \pm 0.0002$, and $g_5 = 2.0029 \pm 0.0002$.

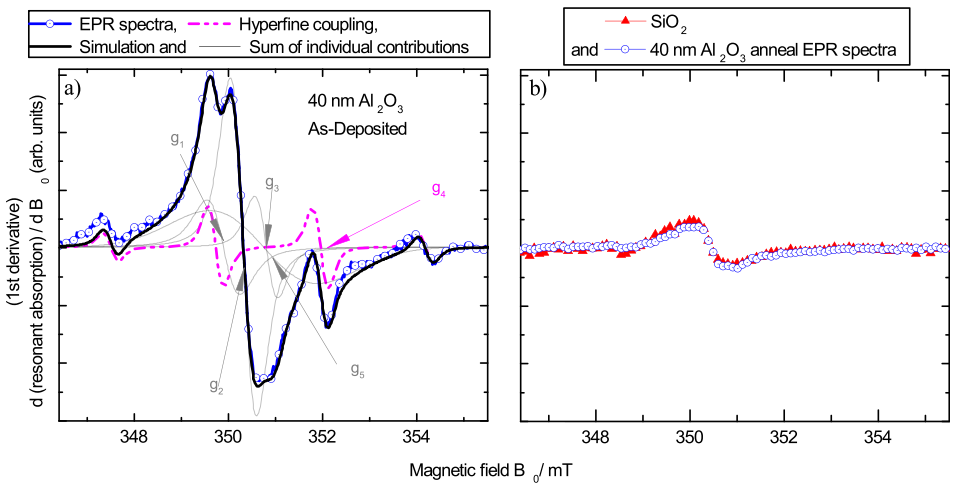

FIG. 4. An EPR spectrum obtained from Si coated with 40 nm of Al_2O_3 without any temperature treatment is shown in (a). The corresponding simulation is plotted using five g values (indicated by g_1 to g_5). (b) EPR signals corresponding to Si coated with a SiO_2 layer with a thickness of 15 nm and Si coated with 40 nm of Al_2O_3 after annealing.

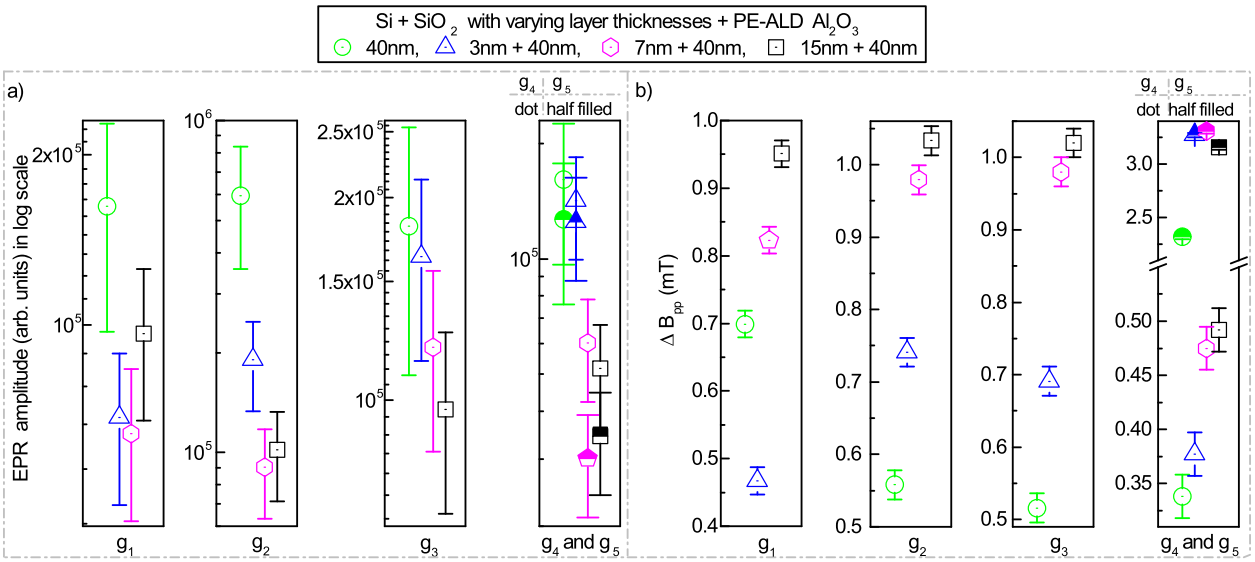

FIG. 5. EPR amplitudes (a) and line width ΔB_{pp} (b) corresponding to g_1, g_2, g_3, g_4 and g_5 for samples with 3 nm to 15 nm interfacial SiO_2 layers between Si and Al_2O_3 and without any additional thermal SiO_2 (*Group 1*). None of the samples underwent any temperature treatment.

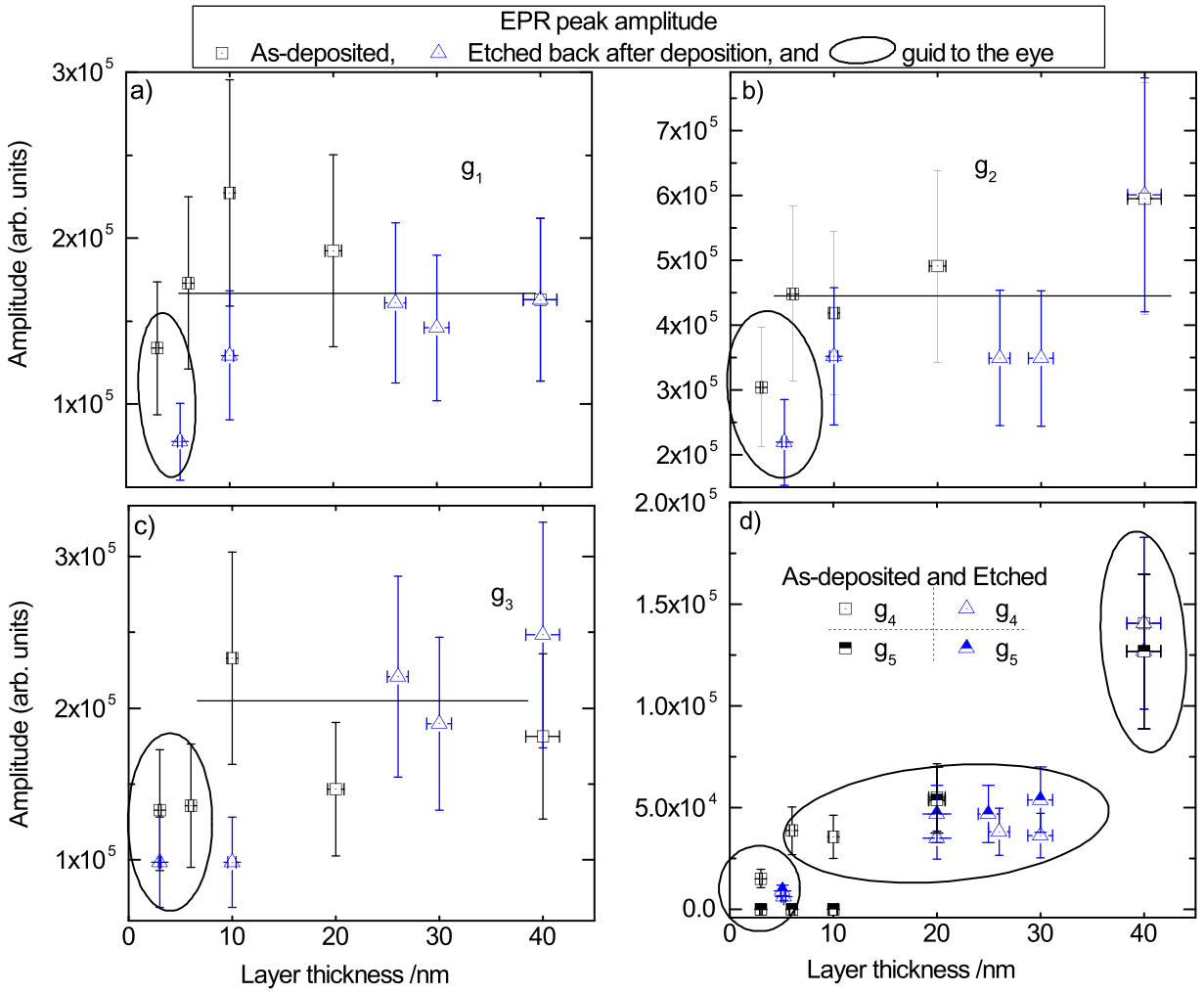

FIG. 6. Amplitudes of the g values as functions of the Al_2O_3 layer thickness for g_1 (a), g_2 (b), g_3 (c), and g_4 and g_5 (d). The black lines are drawn as guides to the eye. The trends are identical for the samples regardless of the method used to achieve the variations in the layer thickness, i.e., different depositions (*Group 2*) or etching a 40 nm Al_2O_3 layer using HF (*Group 3*).

The hyperfine coupling constants result in $A_1 = (2.23 \pm 0.014)$ mT, $A_2 = (2.23 \pm 0.011)$ mT, and $A_3 = (2.23 \pm 0.021)$ mT.

In Figure 5(a), the amplitudes corresponding to the g_1, g_2, g_3, g_4, and g_5 values obtained for the Si/Al_2O_3 samples with and without additional SiO_2 with varying layer thicknesses (*Group 1*) are shown. Based on comparisons of the EPR spectra obtained from Si/Al_2O_3 samples with and without an additional 3 nm interfacial thermal SiO_2 layer, the amplitude of g_2 was detected to decrease by a factor of five. Amplitudes corresponding to g_1, g_4, and g_5 reveal much smaller changes. g_3 seems to be nearly independent of the additional SiO_2 layer. Beside for g_4 and g_5, the changes in the amplitudes of the g values based on comparisons of the interfacial SiO_2 layer thicknesses between the Si and the Al_2O_3 in the range from 3 to 15 nm were not that pronounced. Interestingly, the decrease of amplitudes corresponding to g_4 and g_5 shows nearly identical slopes. The peak-to-peak line width ΔB_{pp} increased for all observed g-values with increasing SiO_2 layer thickness (Figure 5(b)). Comparing ΔB_{pp} for samples with and without an additional SiO_2, the value ΔB_{pp} is almost double that of the previous one for all samples.

The amplitudes for all five g values (g_1, g_2, g_3, g_4, and g_5) are shown as functions of their corresponding Al_2O_3 layer thicknesses (without any temperature treatments) in Figure 6 (*Group 2* and *Group 3*). In addition to the amplitudes corresponding to very thin layers, such as 3 nm to 8 nm, no significant changes in amplitude were detected for g_1, g_2, and g_3, as is evident from Figures 6(a)–6(c). In contrast, changes in amplitude corresponding to g_4 and g_5 with increasing layer thicknesses were observed. Also in this case, the layer thickness dependent changes in amplitude corresponding to g_4 and g_5 show identical slopes.

In addition, all of the described amplitude behaviors were identical for samples with the same layer thicknesses, regardless of whether they were obtained from different deposition times (*Group 2*) or by etching 40 nm Al_2O_3 layers using HF (*Group 3*).

To study the microscopic nature behind the differences in amplitude for layers as thin as 3 nm compared to thicker layers, an Al_2O_3 layer with a thickness of 3 nm was exposed to an oxygen plasma on each side of the wafer and examined by EPR. The EPR amplitudes of g_1, g_2, and g_3 for Al_2O_3 layer thicknesses of 20 nm, 3 nm, and 3 nm with additional plasma treatments are compiled in Table III. After exposing the sample with a 3 nm Al_2O_3 layer to the oxygen plasma, the amplitudes of g_1, g_2, and g_3 increase to the same intensity, which has been observed for 20 nm layers (as shown in Figure 3). The amplitudes corresponding to g_4 and g_5 were not observed for the Al_2O_3 sample with a layer thickness of 3 nm with and without the oxygen plasma treatment.

TABLE III. Amplitudes corresponding to g_1, g_2, and g_3 are shown for Si coated with a 3 nm thick Al_2O_3 layer with and without an additional oxygen plasma treatment (*Group 4*) and for Si coated with 20 nm of Al_2O_3. None of the layers underwent a temperature treatment.

Layer	Amplitude g_1	Amplitude g_2	Amplitude g_3
3 nm	$(11.1 \pm 3.3) \times 10^4$	$(25.3 \pm 7.6) \times 10^4$	$(11.0 \pm 3.3) \times 10^4$
3 nm + Plasma	$(21.5 \pm 6.5) \times 10^4$	$(50.5 \pm 15.2) \times 10^4$	$(23.5 \pm 7.0) \times 10^4$
20 nm	$(19.8 \pm 5.9) \times 10^4$	$(49.6 \pm 14.9) \times 10^4$	$(15.1 \pm 4.5) \times 10^4$

IV. INTERPRETATION AND DISCUSSION

A. *g*-values and their corresponding defects

Without any temperature treatment, five g values ($g_1 = 2.0081 \pm 0.0002$, $g_2 = 2.0054 \pm 0.0002$, $g_3 = 2.0003 \pm 0.0002$, $g_4 = 2.0026 \pm 0.0002$, and $g_5 = 2.0029 \pm 0.0002$) have been detected in Si/Al_2O_3 samples with and without any additional SiO_2 layer in-between. By varying the Al_2O_3 layer thickness, the positions of these dangling bonds can be localized. For Al_2O_3 layer thicknesses above 8nm, the amplitudes of g_1, g_2, and g_3 are independent of the layer thickness. Thus, these signals are attributed to the interface. The amplitudes of g_4 and g_5 decrease with decreasing Al_2O_3 layer thickness. Moreover, both amplitudes (g_4 and g_5) decrease with identical slopes with decreasing Al_2O_3 layer thickness and increasing SiO_2 layer thickness. Hence, g_4 and g_5 probably have the same microscopic origin. Due to the spatial locations of the extracted g values and by comparing these values to those in the literature (see Table I), g_1 and g_3 can be attributed to P_{b0} and g_2 to Si-db (see Table I). The hyperfine pattern corresponding to g_4 arises from three protons that are nearly magnetically equivalent with hyperfine coupling constants of $A_1 = (2.23 \pm 0.014)$ mT, $A_2 = (2.23 \pm 0.011)$ mT, and $A_3 = (2.23 \pm 0.021)$ mT. These hyperfine coupling constants and the corresponding g value fit very well to the average values of methyl radicals in the literature; these values are $A = (2.3 \pm 0.05)$mT and $g = 2.0026 \pm 0.0005$ in γ-ray irradiated amorphous SiO_2 on Si, which was reported by Stesmans, Clémer, and Afanasev, and $A = 2.3$mT and $g = 2.0024$ in solid N_2O, which was reported by Benetis and Dmitriev.[59–63] In amorphous SiO_2, this CH_3 is captured in voids with diameters of around 60nm.[61] Usually, one void captures only a single CH_3 radical.[61] The methyl radicals in the Al_2O_3 layers observed in this contribution can be attributed to the trimethylaluminum precursor material used for the deposition.

The amplitude corresponding to the CH_3 radical signal did not linearly decrease with decreasing Al_2O_3 layer thickness. For Al_2O_3 layer thicknesses smaller than 8 nm, the smallest amplitudes corresponding to g_4 and g_5 were observed (the amplitude is approximately zero). Amplitudes corresponding to g_4 and g_5 were observed to be around five orders of magnitudes higher for Al_2O_3 layer thicknesses thicker than 30 nm. Between 8 nm and 30 nm, the amplitudes corresponding to g_4 and g_5 were observed to be unaffected by changes in the layer thickness. These observations were identical for layer thickness variations obtained by etching a 40 nm Al_2O_3 layer or by varying the Al_2O_3 deposition times. Thus, the voids containing CH_3 radicals seem to be distributed inhomogeneously over the Al_2O_3 bulk. This inhomogeneity might be related to thickness-dependent layer stress of Al_2O_3. Indeed, a correlation between layer thickness and internal layer stress was observed in SiO_2 layers on Si by Au *et al.*[64] Here, the layer stress increases with decreasing layer thickness.[64] Further, a correlation between void density and

layer stress release in carbon films on Si was shown by Puchert *et al.*[65] In this context, it might be interesting to connect these observations to other thickness dependent phenomena known from Al_2O_3 layers like *blistering*.[16,66,67] Here, the density of temperature-induced bubbles within Al_2O_3 layers was observed to increase dramatically with increasing Al_2O_3 layer thickness.[16,66,67] Thus, the higher void density observed in this contribution for thick Al_2O_3 layers might lead to a higher capture probability for hydrogen components. With increasing temperature, the gas pressure might increase within these voids until they are destroyed. This suggestion gets underlined by the following observation; blisters in PECVD deposited Al_2O_3 layers of more than 20 nm layer thicknesses form without affecting the passivation quality.[68] This observation shows that the bubble nucleation does not occur at the interface. Thus, we propose that the upper parts of thick Al_2O_3 layers contain voids with CH_3 radicals, which might later transform into nucleation cites for blistering.

B. Q_{tot}, D_{it} and paramagnetic moments during annealing

With a temperature treatment at 450 °C for 5 min, the signals from all of the paramagnetic moments disappear, the value of D_{it} decreases, and Q_{tot} increases slightly. Thus, in contrast to D_{it}, Q_{tot} does not correlate with any paramagnetic moment. The observed connection between P_{b0} and D_{it} is consistent with results obtained for Si/SiO_2 interfaces.[29] In addition, also for Si/SiO_2 interfaces, no correlation between fixed charges Q_{tot} and paramagnetic moments was observed.[69] The disappearance of the CH_3 signal might be connected to the effusion or its oxidation within the Al_2O_3 layer of this component.[70]

Thus, D_{it} is probably at least partly related to Si-db and P_{b0} traps. Hence, the decrease in D_{it} might partly be explained by the saturation of the P_{b0} defects with hydrogen, which was suggested by Dingemans and Kessels.[1] As mentioned before, Si-dbs are related to amorphous Si. Thus, the disappearance of the Si-db signal after annealing might be related to Si surface oxidation or restructuring and might also be related to the decrease in D_{it}. Based on these observations and interpretations so far, the microscopic model suggested by Kühnhold-Pospischil *et al.* to explain the origin of Q_{tot} and its possible connection to D_{it} can be applied;[19] before annealing, Si-dbs and P_{b0} defects located within the intrinsic SiO_x layer are unoccupied, and electrons can move via defects from Si to point defects in Al_2O_3.[19] The un-passivated Si-dbs and P_{b0} defects reveal the observed paramagnetic signal. The absent paramagnetic moment of Q_{tot} can be explained by the model of Fonseca, Liu, and Robertson.[11] Here, a negative correlation energy has been proposed for oxygen interstitials (see Figure 7(a)).[11] During annealing, the defect-based electron transport is enhanced, which results in the slight increase in Q_{tot}. At the same time, an increasing number of hydrogen atoms occupy Si-db and P_{b0} defects during annealing. Thus, with an increasing number of hydrogen atoms occupying Si-dbs and P_{b0} defects, the electron transport via defects becomes more and more hindered during annealing. In addition, the electron transfer is also reduced by the band bending induced by Q_{tot}, which repels electrons from the Si surface (see Figure 7(b)). The microscopic model for Q_{tot} and D_{it} is summarized in the illustration in Figure 7.

C. The $Si/SiO_2/Al_2O_3$ interface

As shown by the COCOS measurements (see Figures 2(a) and 2(b)), high Q_{tot} and D_{it} values were detected after

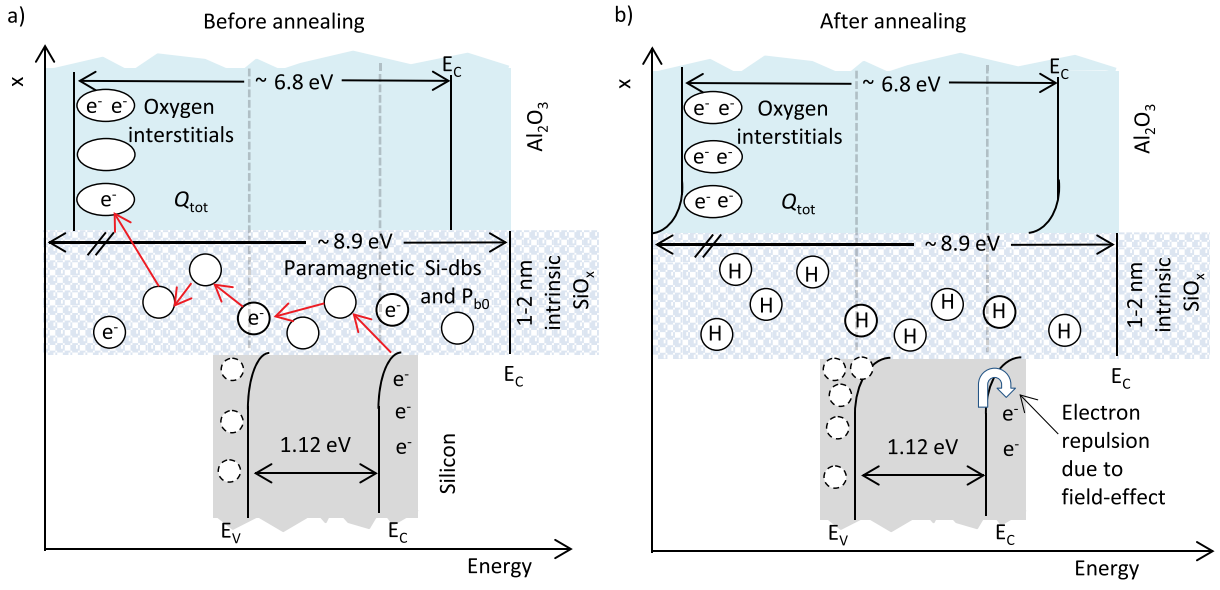

FIG. 7. Model of the Si/Al_2O_3 interface after Kühnhold-Pospischil *et al.*[19] Dashed circles represent holes in the Si valence band, continuous lined circles represent Si-dbs and P_{b0} defects, and ovals represent oxygen interstitials. (a) After deposition, unoccupied Si-dbs and P_{b0} defects provide free paths for electrons to hop from Si to oxygen interstitials within Al_2O_3. Paramagnetism is shown for electrons occupying Si-dbs and P_{b0} defects. (b) During annealing, Si-dbs and P_{b0} defects are passivated by hydrogen atoms (indicated by H), which prevent electrons from hopping. Furthermore, the charged oxygen interstitials lead to band bending, which leads to the repulsion of electrons. Oxygen interstitials have a negative correlation energy, which leads to the absence of paramagnetism related to Q_{tot}.

deposition (without any temperature treatment) at the interface of the PE-Al_2O_3 on Si. When applying a thermally grown SiO_2 layer between the Si and the Al_2O_3, both densities decrease by about one order of magnitude. As demonstrated by the FTIR results, the molecular structure of the Al_2O_3 is identical for samples with and without an additional thermally grown SiO_2 between the Si and the Al_2O_3. Moreover, the vibrations related to hydrogen and carbon do not show significant changes in the FTIR spectra of Al_2O_3 with and without an additional SiO_2 layer. The wavenumber range observed for the FTIR peaks, which can be correlated with the SiO_2 intrinsically grown at the Si/Al_2O_3 interface (see Figure 3(a)), is 900 cm^{-1} till 1300 cm^{-1}), is similar to that of the SiO_2 layer thermally grown between Si and Al_2O_3. Hence, the molecular structures of SiO_2 for samples with and without an additional thermally grown SiO_2 layer are similar. Thus, the changes in D_{it} and Q_{tot} induced by an additional thermally grown SiO_2 layer between the Si and the Al_2O_3 cannot be explained by molecular changes.

In contrast, with an additional SiO_2 layer between the Si and the Al_2O_3, the amplitude of g_2 (Si-db) decreased in analogy to D_{it} by about one order of magnitude; the changes in amplitude for g_1, g_3, and g_4 were less significant. Two conclusions can be made upon these observations; first, the D_{it} at the Si/Al_2O_3 interface seems to be dominated by Si-db and second, due to the different behavior of Si-db and P_{b0} defects with increasing SiO_2 layer, the microscopic origins of both defects seem to be different. The second statement might be connected with Section IV D 1.

D. Interaction between Al_2O_3 and the Si/SiO_2 interface

Si/SiO_2 samples did not reveal any paramagnetic moment. In contrast, the same sample structure stacked with an additional Al_2O_3 layer showed P_{b0}, Si-db, and CH_3 defects. Thus, even with a SiO_2 layer with a maximum layer thickness of 15 nm separating Si and Al_2O_3, Al_2O_3 causes interface defects between Si/SiO_2. In principle, one of the two mechanisms exists to explain this observation: one is based on an indirect interaction mechanism and the other on a direct interaction mechanism between the Al_2O_3 and Si/SiO_2 interface.

1. Indirect interaction mechanism

One possibility is that the plasma exposure during the Al_2O_3 deposition process causes these defects. This explanation is confirmed by the following observation: amplitudes corresponding to g values obtained from Al_2O_3 layers thinner than 8 nm differ from amplitudes corresponding to thicker layers. The exposure of a sample with a 3 nm Al_2O_3 layer to oxygen plasma results in increases in the amplitudes corresponding to g_1, g_2, and g_3. These amplitudes are identical for layers thicker than 8 nm.

As discussed above, with an additional SiO_2 layer between the Si and the Al_2O_3, the amplitude of g_2 (Si-db) decreased by about one order of magnitude; the changes in amplitude for g_1 and g_3 were less significant. As shown earlier, P_{b0} defects can be assigned to damages induced by high energetic photons and Si-db by mechanical damages.

Thermal SiO_2 is transparent for electromagnetic wavelengths till 400 nm.[71] For wavelengths below 400 nm, the extinction coefficient increases slowly.[71] Thus, the additional thermal SiO_2 between Al_2O_3 and Si might protect the Si surface against high energetic particles originating from the oxygen plasma but high energetic photons might penetrate through this SiO_2 layer. Hence, the additional SiO_2 layer might reduce mechanical damages on the Si surface but not surface damages induced by high energetic photons. This mechanism is illustrated in Figure 8.

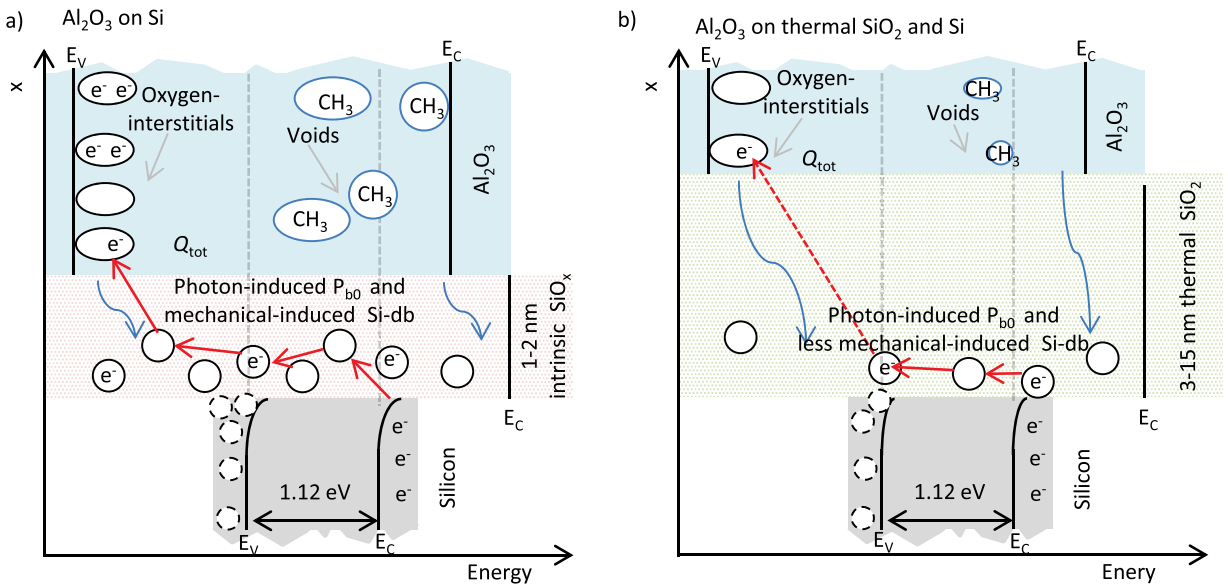

FIG. 8. Model of the Si/Al_2O_3 interface in (a) and the $Si/SiO_2/Al_2O_3$ interfaces in (b) without annealing. Dashed circles represent holes in the Si valence band, continuous lined circle Si-dbs and P_{b0} defects, ovals (black) represent oxygen interstitials and ovals (blue) voids. The blue arrows represent high energetic photons originating from the oxygen plasma. SiO_2 is transparent for high energetic photons. Thus, an additional SiO_2 might protect the Si surface against high energetic particles but not against high energetic photons. Hence, P_{b0} are possibly caused by high energetic photons and Si-db by high energetic particles. Further, the decreasing defect density with increasing SiO_2 layer thickness might reduce the probability for the defect based electron transport leading to Q_{tot}.

2. Direct interaction mechanism

Another possible explanation to the connection between Al_2O_3 and defects at the Si/SiO_2 interface might directly be related to Al_2O_3. For example, Al_2O_3 might deform the SiO_2 layer which might lead to the observed dangling bonds between Si and SiO_2. Another possibility might be that components from Al_2O_3 diffuse to the Si/SiO_2 interface and lead to the observed defect structure. Interestingly, such observations have been made by Jin, Weber, and Smith.[72] First, Jin, Weber, and Smith deposited a thermal SiO_2 layer with 50 nm layer thickness onto a wafer and recorded the corresponding EPR spectra.[72] After that, they deposited an additional SiN_x layer on top of these samples using a CVD deposition technique.[72] Jin, Weber, and Smith recorded again the EPR spectra and observed an increase in amplitudes attributed to P_b defects and an increase in the corresponding line widths ΔB_{pp}.[72] After that, they removed the SiN_x but the defect structure kept constant.[72] Jin, Weber, and Smith explained this observation by the diffusion of N through the SiO_2 layer.[72] N is known to cause P_b-like defects at the Si/SiN_x interface, called P_{bN}.[73] Further, N has a relatively high diffusion constant in SiO_2.[74] Whether this explanation can be extended to the observed influence of Al_2O_3 on the Si/SiO_2 interface is questionable; for example, Al shows an activation energy for diffusion in SiO_2 of $E_A \approx 5 \times 10^{10}$ eV which is significantly higher compared to the value of N.[75,76] Moreover, Al is not known to cause Si/Al_2O_3 interface defects which are behaving similar to P_b.

Hence, an explanation based on SiO_2 layer stress induced by Al_2O_3 might be more realistic. Indeed, a correlation between layer tension and interface defects was discussed for SiN_x layers on Si.[77]

Further studies are needed to distinguish between the proposed indirect and direct interaction models describing the interaction between Al_2O_3 and Si/SiO_2 interface.

V. CONCLUSION

Without any temperature treatment, paramagnetic moments related to Si-dbs, P_{b0}, and CH_3 were detected in $Si/(SiO_2)/Al_2O_3$. After a temperature treatment at 450 °C for 5 min in ambient air, all of the paramagnetic moments disappear, which can be explained by the saturation of these defects by hydrogen, oxygen, and the effusion of CH_3. At the same time, D_{it} decreases, while Q_{tot} increases slightly. Thus, at least some of D_{it} can be explained by Si-dbs and P_{b0} defects. In contrast, Q_{tot} does not correlate with any paramagnetic moment. As suggested by Kühnhold-Pospischil *et al.*, a defect-based electron transport mechanism might lead to Q_{tot} and would explain these observations.[19] Here, electrons from Si reach defects within Al_2O_3 via interface defects. Without annealing, these transport defects reveal the observed paramagnetic moments. During annealing, all paramagnetic moments disappear due to the saturation of these dangling bonds. With this saturation of dangling bonds, the electron defect transport is hindered.

When adding an additional thermally grown SiO_2 layer at the Si/Al_2O_3 interface, D_{it} and Q_{tot} change by about one order of magnitude. For layers without any temperature treatment, the same was observed for the amplitude corresponding to the Si-dbs. The changes in amplitude corresponding to P_{b0} defects were less pronounced. Thus, the D_{it} at the Si/Al_2O_3 is dominated by Si-db and further, the microscopic origin of Si-db and P_{b0} defects is different.

Moreover, the microscopic nature behind the Si-dbs and the P_{b0} centers is probably related to the oxygen plasma process during the Al_2O_3 ALD deposition. Possibly, high energetic photons cause P_{b0} defects and high energetic particles the surface damages called Si-dbs.

ACKNOWLEDGMENTS

S.K. was supported by the DFG (Deutsche Forschungsgemeinschaft) under Grant Nos. WE3861/2-1, EL155/25-1 and WE2376/5-1. We thank all colleagues who supported this work at the Fraunhofer ISE and the Institute of Physical Chemistry of the University of Freiburg.

[1]G. Dingemans and W. Kessels, J. Vac. Sci. Technol. A **30**, 040802 (2012).
[2]B. Hoex, S. Heil, E. Langereis, M. C. M. van de Sanden, and W. M. M. Kessels, Appl. Phys. Lett. **89**, 042112 (2006).
[3]A. W. Blakers, A. Wang, A. M. Milne, J. Zhao, and M. A. Green, Appl. Phys. Lett. **55**, 1363–1365 (1989).
[4]J. H. Petermann, D. Zielke, J. Schmidt, F. Haase, E. G. Rojas, and R. Brendel, Prog. Photovoltaics: Res. Appl. **20**, 1–5 (2012).
[5]J. Schmidt, A. Merkle, R. Brendel, B. Hoex, M. Van de Sanden, and W. Kessels, Prog. Photovoltaics: Res. Appl. **16**, 461–466 (2008).
[6]J. Benick, B. Hoex, M. Van de Sanden, W. Kessels, O. Schultz, and S. W. Glunz, Appl. Phys. Lett. **92**, 253504 (2008).
[7]S. Guha, E. Cartier, N. Bojarczuk, J. Bruley, L. Gignac, and J. Karasinski, J. Appl. Phys. **90**, 512–514 (2001).
[8]B. Hoex, J. Schmidt, R. Bock, P. Altermatt, M. Van de Sanden, and W. Kessels, Appl. Phys. Lett. **91**, 112107 (2007).
[9]B. Hoex, J. Gielis, M. Van de Sanden, and W. Kessels, J. Appl. Phys. **104**, 113703 (2008).
[10]G. Dingemans, W. Beyer, M. Van de Sanden, and W. Kessels, Appl. Phys. Lett. **97**, 152106 (2010).
[11]L. Fonseca, D. Liu, and J. Robertson, Appl. Phys. Lett. **93**, 122905 (2008).
[12]J. A. Töfflinger, A. Laades, L. Korte, C. Leendertz, L. M. Montañez, U. Stürzebecher, H.-P. Sperlich, and B. Rech, Sol. Energy Mater. Sol. Cells **135**, 49–56 (2015).
[13]V. Naumann, M. Otto, R. Wehrspohn, M. Werner, and C. Hagendorf, Energy Proc. **27**, 312–318 (2012).
[14]K. Kimoto, Y. Matsui, T. Nabatame, T. Yasuda, T. Mizoguchi, I. Tanaka, and A. Toriumi, Appl. Phys. Lett. **83**, 4306 (2003).
[15]B. Hoex, M. Bosman, N. Nandakumar, and W. Kessels, Phys. Status Solidi (RRL) **7**, 937–941 (2013).
[16]S. Kühnhold, P. Saint-Cast, B. Kafle, M. Hofmann, F. Colonna, and M. Zacharias, J. Appl. Phys. **116**, 054507 (2014).
[17]G. Dingemans, N. Terlinden, M. Verheijen, M. Van de Sanden, and W. Kessels, J. Appl. Phys. **110**, 093715 (2011).
[18]S. Mack, A. Wolf, C. Brosinsky, S. Schmeisser, A. Kimmerle, P. Saint-Cast, M. Hofmann, and D. Biro, IEEE J. Photovoltaics **1**, 135–145 (2011).
[19]S. Kühnhold-Pospischil, P. Saint-Cast, A. Richter, and M. Hofmann, Appl. Phys. Lett. **109**, 061602 (2016).
[20]P. Anderson, Phys. Rev. Lett. **34**, 953 (1975).
[21]D. Adler and E. J. Yoffa, Phys. Rev. Lett. **36**, 1197 (1976).
[22]B. Moyzhes, T. H. Geballe, S. Jeong, D. Gitlin, and J. Karp, J. Appl. Phys. **97**, 074104 (2005).
[23]S. E. Curry, P. Lenahan, D. Krick, J. Kanicki, and C. Kirk, "Evidence for a negative electron-electron correlation energy in the dominant deep trapping center in silicon nitride films," Appl. Phys. Lett. **56**, 1359–1361 (1990).
[24]J. E. Northrup and J. Neugebauer, Phys. Rev. B **57**, R4230 (1998).
[25]B. Jones and R. Barklie, Microelectron. Eng. **80**, 74–77 (2005).
[26]J. Cantin and H. Von Bardeleben, J. Non-Cryst. Solids **303**, 175–178 (2002).
[27]S. Baldovino, S. Nokhrin, G. Scarel, M. Fanciulli, T. Graf, and M. Brandt, J. Non-Cryst. Solids **322**, 168–173 (2003).

[28]P. Lenahan and J. Conley, Jr., J. Vac. Sci. Technol. B **16**, 2134–2153 (1998).
[29]P. Lenahan and P. Dressendorfer, J. Appl. Phys. **54**, 1457–1460 (1983).
[30]G. Walters and T. Estle, J. Appl. Phys. **32**, 1854–1859 (1961).
[31]C. Herzinger, B. Johs, W. McGahan, J. Woollam, and W. Paulson, J. Appl. Phys. **83**, 3323–3336 (1998).
[32]J. A. Woollam, B. D. Johs, C. M. Herzinger, J. N. Hilfiker, R. A. Synowicki, and C. L. Bungay, "Overview of variable-angle spectroscopic ellipsometry (VASE): I. Basic theory and typical applications," in *Optical Metrology* (the Society of Photo-Optical Instrumentation Engineers, 1999), Vol. 1, pp. 3–28.
[33]B. D. Johs, J. A. Woollam, C. M. Herzinger, J. N. Hilfiker, R. A. Synowicki, and C. L. Bungay, "Overview of variable-angle spectroscopic ellipsometry (VASE): II. Advanced applications," in *Optical Metrology* (the Society of Photo-Optical Instrumentation Engineers, 1999), pp. 29–58.
[34]D. Smith, M. Inokuti, and W. Karstens, J. Phys.: Condens. Matter **13**, 3883 (2001).
[35]A. Richter, Ph.D. thesis (Fraunhofer Verl., 2015).
[36]M. Wilson, J. Lagowski, A. Savtchouk, L. Jastrzebski, and J. D'Amico, in *Gate Dielectric Integrity: Material, Process, and Tool Qualification* (ASTM International, 2000).
[37]D. Schuldis, A. Richter, J. Benick, and M. Hermle, in Proceedings of the 27th European PV Solar Energy Conference and Exhibition (2012), pp. 24–28.
[38]Z. Xin, S. Duttagupta, M. Tang, Z. Qiu, B. Liao, A. G. Aberle, and R. Stangl, IEEE J. Photovoltaics **6**, 1080–1089 (2016).
[39]A. Cuevas, M. Stocks, D. Macdonald, and R. Sinton, *Applications of the Quasi-steady-state Photoconductance Technique* (The Australian National University, 1998).
[40]A. L. Blum, J. S. Swirhun, R. A. Sinton, F. Yan, S. Herasimenka, T. Roth, K. Lauer, J. Haunschild, B. Lim, K. Bothe *et al.*, IEEE J. Photovoltaics **4**, 525–531 (2014).
[41]A. Stesmans and G. Van Gorp, Phys. Lett. A **139**, 95–98 (1989).
[42]S. Stoll and A. Schweiger, J. Magn. Reson. **178**, 42–55 (2006).
[43]M. Wojdyr, J. Appl. Crystallogr. **43**, 1126–1128 (2010).
[44]A. Richter, J. Benick, M. Hermle, and S. W. Glunz, Appl. Phys. Lett. **104**, 061606 (2014).
[45]R. Katamreddy, R. Inman, G. Jursich, A. Soulet, and C. Takoudis, J. Electrochem. Soc. **153**, C701–C706 (2006).
[46]A. R. Chowdhuri, C. G. Takoudis, R. Klie, and N. Browning, Appl. Phys. Lett. **80**, 4241–4243 (2002).
[47]P. Tarte, Spectrochim. Acta, Part A **23**, 2127–2143 (1967).
[48]C. Morterra and G. Magnacca, Catal. Today **27**, 497–532 (1996).
[49]A. Dillon, A. Ott, J. Way, and S. George, Surf. Sci. **322**, 230–242 (1995).
[50]P. V. Bulkin, P. L. Swart, and B. M. Lacquet, J. Non-Cryst. Solids **226**, 58–66 (1998).
[51]L. Yi, J. Heitmann, R. Scholz, and M. Zacharias, J. Phys.: Condens. Matter **15**, S2887 (2003).
[52]S. M. Han and E. S. Aydil, Appl. Phys. Lett. **70**, 3269–3271 (1997).
[53]C. Kirk, Phys. Rev. B **38**, 1255 (1988).
[54]Y.-C. Kim, H.-H. Park, J. S. Chun, and W.-J. Lee, Thin Solid Films **237**, 57–65 (1994).
[55]D. N. Goldstein, J. A. McCormick, and S. M. George, J. Phys. Chem. C **112**, 19530–19539 (2008).
[56]T. O. Kääriäinen and D. C. Cameron, Plasma Processes Polym. **6**, S237–S241 (2009).
[57]A. R. McInroy, D. T. Lundie, J. M. Winfield, C. C. Dudman, P. Jones, and D. Lennon, Langmuir **21**, 11092–11098 (2005).
[58]E. Langereis, J. Keijmel, M. Van de Sanden, and W. Kessels, Appl. Phys. Lett **92**, 231904–231906 (2008).
[59]A. Stesmans, K. Clémer, and V. Afanasev, Phys. Rev. B **72**, 155335 (2005).
[60]N. P. Benetis and Y. Dmitriev, J. Phys. Chem. A **117**, 4233–4250 (2013).
[61]G. Buscarino, S. Agnello, F. Gelardi, and R. Boscaino, J. Non-Cryst. Solids **361**, 9–12 (2013).
[62]W. R. Austin and R. Leisure, J. Appl. Phys. **80**, 6646–6650 (1996).
[63]E. Friebele, D. Griscom, and K. Rau, J. Non-Cryst. Solids **57**, 167–175 (1983).
[64]V. Au, C. Charles, D. Bulla, J. Love, and R. Boswell, J. Appl. Phys. **97**, 84912 (2005).
[65]M. Puchert, P. Timbrell, R. Lamb, and D. McKenzie, J. Vac. Sci. Technol. A **12**, 727–732 (1994).
[66]B. Vermang, H. Goverde, A. Lorenz, A. Uruena, G. Vereecke, J. Meersschaut, E. Cornagliotti, A. Rothschild, J. John, J. Poortmans *et al.*, in *Proceedings of the 37th IEEE Photovoltaic Specialists Conference (PVSC)* (IEEE, 2011), pp. 003562–003567.
[67]P. Saint-Cast, D. Kania, R. Heller, S. Kuehnhold, M. Hofmann, J. Rentsch, and R. Preu, Appl. Surf. Sci. **258**, 8371–8376 (2012).
[68]P. Saint-Cast, "Passivation of Si surfaces by PECVD aluminum oxide," Ph.D. thesis (2012).
[69]P. J. Caplan, E. H. Poindexter, B. E. Deal, and R. R. Razouk, J. Appl. Phys. **50**, 5847–5854 (1979).
[70]G. Dingemans, P. Engelhart, R. Seguin, F. Einsele, B. Hoex, M. Van de Sanden, and W. Kessels, J. Appl. Phys. **106**, 114907 (2009).
[71]L. Gao, F. Lemarchand, and M. Lequime, Opt. Express **20**, 15734–15751 (2012).
[72]H. Jin, K. J. Weber, and P. J. Smith, Appl. Phys. Lett. **89**, 092120 (2006).
[73]A. Stesmans and G. Van Gorp, Phys. Rev. B **52**, 8904 (1995).
[74]A. Van Ommen, Appl. Surf. Sci. **30**, 244–264 (1987).
[75]E. Cavanagh, J. Franco, and N. W. de Reca, Jpn. J. Appl. Phys. **15**, 1803 (1976).
[76]O. Jintsugawa, M. Sakuraba, T. Matsuura, and J. Murota, Surf. Interface Anal. **34**, 456–459 (2002).
[77]Y.-G. Jung, A. Pajares, and B. R. Lawn, J. Mater. Res. **19**, 3569–3575 (2004).